AGU PUBLICATIONS

JGR

Journal of Geophysical Research: Atmospheres

RESEARCH ARTICLE
10.1002/2015JD024633

Key Points:
- Spectral nudging enabled comparisons between model runs with differing physical processes
- The surface wind speeds were directly related to the warm core of the polar low
- With surface fluxes switched off, the warm core dissipated and wind speeds were lower

Correspondence to:
E. W. Kolstad,
erik.kolstad@uni.no

Citation:
Kolstad, E. W., T. J. Bracegirdle, and M. Zahn (2016), Re-examining the roles of surface heat flux and latent heat release in a "hurricane-like" polar low over the Barents Sea, *J. Geophys. Res. Atmos.*, *121*, 7853–7867, doi:10.1002/2015JD024633.

Received 10 DEC 2015
Accepted 24 JUN 2016
Accepted article online 30 JUN 2016
Published online 12 JUL 2016

Re-examining the roles of surface heat flux and latent heat release in a "hurricane-like" polar low over the Barents Sea

Erik W. Kolstad[1], Thomas J. Bracegirdle[2], and Matthias Zahn[3]

[1]Uni Research Climate, Bjerknes Centre for Climate Research, Bergen, Norway, [2]British Antarctic Survey, Cambridge, UK, [3]Helmholtz-Zentrum Geesthacht, Geesthacht, Germany

Abstract Polar lows are intense mesoscale cyclones that occur at high latitudes in both hemispheres during winter. Their sometimes evidently convective nature, fueled by strong surface fluxes and with cloud-free centers, have led to some polar lows being referred to as "arctic hurricanes." Idealized studies have shown that intensification by hurricane development mechanisms is theoretically possible in polar winter atmospheres, but the lack of observations and realistic simulations of actual polar lows have made it difficult to ascertain if this occurs in reality. Here the roles of surface heat fluxes and latent heat release in the development of a Barents Sea polar low, which in its cloud structures showed some similarities to hurricanes, are studied with an ensemble of sensitivity experiments, where latent heating and/or surface fluxes of sensible and latent heat were switched off before the polar low peaked in intensity. To ensure that the polar lows in the sensitivity runs did not track too far away from the actual environmental conditions, a technique known as spectral nudging was applied. This was shown to be crucial for enabling comparisons between the different model runs. The results presented here show that (1) no intensification occurred during the mature, postbaroclinic stage of the simulated polar low; (2) surface heat fluxes, i.e., air-sea interaction, were crucial processes both in order to attain the polar low's peak intensity during the baroclinic stage and to maintain its strength in the mature stage; and (3) latent heat release played a less important role than surface fluxes in both stages.

1. Introduction

The open waters of the Nordic Seas are one of the main breeding grounds of polar lows [*Rasmussen and Turner*, 2003], an intense subset of polar mesocyclones. Many polar lows form over the Barents Sea [*Rasmussen*, 1985; *Wilhelmsen*, 1985; *Ese et al.*, 1988; *Blechschmidt*, 2008; *Kolstad*, 2015; *Smirnova et al.*, 2015], which is largely ice-free even in the depth of winter.

Polar lows over the Nordic Seas are most common during the colder months from November to March [*Wilhelmsen*, 1985; *Bracegirdle and Gray*, 2008; *Noer and Saetra*, 2011]. Large air-sea temperature differences and horizontal gradients in surface conditions contribute to the rich diversity in their structure. The strong baroclinicity in some cases can be partially attributed to sharp horizontal contrasts between snow- and ice-covered regions and areas of relatively warm open ocean. The flow of cold air from ice- and snow-covered regions to relatively warm ice-free ocean surfaces also triggers strong surface heat fluxes, convection, and latent heating, which can have a profound impact on polar low characteristics [*Økland*, 1987; *Bresch et al.*, 1997; *Yanase et al.*, 2004].

It has become clear that these different influences result in a "spectrum" of dynamical mechanisms broadly ranging from mainly baroclinic dynamics through to polar lows driven mainly by convection [*Rasmussen and Turner*, 2003]. *Yanase and Niino* [2007] showed, using an idealized model setup, that the transition between baroclinic systems (often associated with comma clouds) and barotropic systems (with more axisymmetric vortices), is quite smooth. In fact, polar lows often initiate through mainly baroclinic processes before surface fluxes, convection, low static stability, and latent heating become more important later in their life cycle [*Nordeng*, 1990; *Montgomery and Farrell*, 1992; *Nielsen*, 1997; *Bracegirdle and Gray*, 2009]. It is during their postbaroclinic, convective stages that polar lows sometimes exhibit structures reminiscent of hurricanes (i.e., tropical cyclones) [*Rasmussen*, 1979], albeit on a considerably smaller spatial scale, with a clear central eye surrounded by spiral bands of convective cloud, giving rise to the term "arctic hurricane" [*Emanuel and Rotunno*, 1989].

When examining the most extreme small-scale wind episodes in the Barents Sea, *Kolstad* [2015] found that large Eady growth rates [*Lindzen and Farrell*, 1980; *Hoskins and Valdes*, 1990], i.e., low-level baroclinicity, and high surface heat fluxes were the clearest precursors 24 h before the peaks of the episodes. The most extreme events had larger differences between the SSTs and the air temperature than the somewhat less extreme events, both before and during their peaks. In other words, strong baroclinicity can produce cyclones with high wind speeds, but the most extreme winds usually form when the baroclinic conditions are embedded in strong marine cold air outbreaks (MCAOs) [*Kolstad et al.*, 2009]. Low static stability is also one of the key mechanisms for the formation of explosive marine cyclones [*Wang and Rogers*, 2001] and sting jets [*Schultz and Sienkiewicz*, 2013].

Here we study a long-lasting polar low which initiated through a rapid baroclinic development starting on 18 December 2002 over the Barents Sea and which exhibited hurricane-like characteristics during the later stages of its life cycle. On the 18th, the maximum vertical difference between the SST and the temperature at 800 hPa, an indicator used for evaluating the strength of MCAOs [*Fletcher et al.*, 2016], reached its fifth highest wintertime value in 1979–2015 over the Barents Sea, according to the ERA-Interim reanalysis [*Dee et al.*, 2011]. This shows that the polar low formed in an extreme MCAO, and the potential for extremely strong ocean-atmosphere heat fluxes, was present.

A numerical model simulation of the same case as the one studied here was conducted by *Føre et al.* [2012]—referred to as *F12* from now on—and showed some evidence for hurricane-like mechanisms in the later stages. However, their simulated polar low made landfall about 24 h too early. It is therefore possible that the simulation underestimated the real intensity of the polar low in later stages. This is a key motivation for returning to this case here, with the aim of producing a more accurate simulation of the later stages to help better quantify the key driving mechanisms during the mature phase of the polar low's life cycle.

Idealized simulations suggest that intensification by mechanisms of hurricane development is possible in arctic conditions owing to the large combined sensible and latent ocean-atmosphere heat fluxes that can occur [*Emanuel and Rotunno*, 1989; *Yanase and Niino*, 2005, 2007]. It seems highly unlikely that such conditions could be sustained for long enough for intensification into a mature hurricane (which takes around five days), due in part to the limited spatial extent of the Nordic seas. However, the Coriolis force is large at high latitudes, enabling faster growth [e.g., *Terpstra et al.*, 2015], so shorter periods of such intensification could conceivably increase the strength and extend the lifetime of polar lows in their mature phase. The extent to which this occurs in nature has been difficult to determine due to challenges associated both with observing and simulating polar lows. It is possible that although the air-sea temperature differences are large, the sea surface temperatures (SSTs) are too modest in typical polar low regions. For instance, when studying a hurricane-like polar low over Hudson Bay, the numerical model used by *Albright et al.* [1995] was only able to produce hurricane-force wind speeds when the SSTs were increased by 8 K.

As the sea ice extent in the Barents Sea region has decreased in recent years [*Screen and Simmonds*, 2010; *Onarheim et al.*, 2015], and is projected to decrease further in the future [*Koenigk et al.*, 2011; *Bracegirdle and Stephenson*, 2012; *Koenigk et al.*, 2013], the maritime activity in the region is likely to increase. But these physical changes are also likely to change the spatial and temporal resolution of polar lows. In a study based on dynamical downscaling, *Zahn and von Storch* [2010] found a projected future decrease in the frequency of polar lows in the Nordic Seas region, in general, although this was more evident for the southern part of the region than for the Barents Sea. They linked this decrease to more stable atmospheric conditions on average, because the midlevel atmosphere in the Arctic is projected to warm faster than the ocean surface. Qualitatively similar projections have been made for the North Pacific [*Chen et al.*, 2014]. *Kolstad and Bracegirdle* [2008] found a strong projected increase in MCAOs, in which polar lows form, over the northeast Barents Sea as the ocean surface, which was previously covered by sea ice, becomes exposed, allowing stronger surface fluxes of sensible and latent heat that fuel polar lows and other cyclones in the Arctic [*Simmonds and Keay*, 2009]. The uncertainties in previous research on this topic, and the projected increase in commercial activity in the Barents Sea region, mean that it is more important than ever to understand the role of diabatic forcing in the development of polar lows.

There are four main differences between our study and *F12*. First, and perhaps most importantly, we used spectral nudging [*von Storch et al.*, 2000; *Miguez-Macho et al.*, 2004] to keep the storm track of the polar low in the simulations close to the observed track. Spectral nudging was not used in *F12*, and the

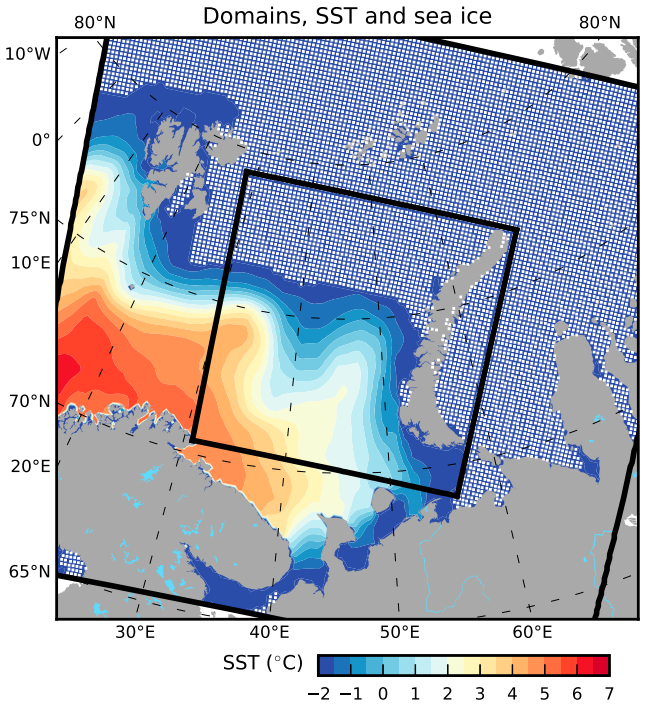

Figure 1. Model domains and prescribed lower boundary conditions. The black boxes show the two model domains, the filled contours show SSTs in °C (see color bar), and the white squares indicate sea ice. Inside the inner domain, the SSTs are also shown with black contours every 0.5°C (negative isolines dashed, zero and positive isolines solid).

discrepancies between the different model runs are obvious in their Figure 8, which shows that the polar low in their control run developed far away from those in the sensitivity runs. The reason for this is simple. When nudging is not applied, the polar low developments in each run are solely dependent on the model physics and the initial and boundary conditions from the underlying data. Such a setup is sensitive to small disturbances, either in the initial field or in the model formulation. The latter may be introduced when the model routines are altered, e.g., when latent heating is switched off in sensitivity studies. Such changes may cause random impacts either on the model's large-scale conditions or more locally on the polar low and its environment.

The remaining three differences compared to *F12* are the following: (1) The effects of condensational heating were investigated differently. (2) We used a different planetary boundary layer (PBL) scheme than the one used in *F12*. (3) We initialized the model runs 12 h later, yielding a polar low development that corresponded better with satellite-based observations.

2. Methods

2.1. Model Setup

We used version 3.5.1 of the Weather Research and Forecasting (WRF) model [*Skamarock and Klemp*, 2008], forced with global ERA-Interim reanalysis data [*Dee et al.*, 2011]. Figure 1 shows the geographical extents of the two model domains. The inner domain had a resolution of 3 km (the same as in *F12*) and covered the region where the polar low developed. It was nested inside a 15 km domain. There were 41 vertical levels, with an increasingly high resolution toward the surface; the 24 lowest levels were all below the 700 hPa surface. The time step was 6 times the horizontal resolution, i.e., 90 and 18 s for the two domains, respectively. Feedback between the domains was switched on.

In the control run, which we will refer to as *ctrl*, we used Thompson's microphysics scheme [*Thompson et al.*, 2008], the Noah land surface model [*Tewari et al.*, 2004], the Mellor-Yamada-Nakanishi-Niino (MYNN) planetary boundary layer scheme [*Nakanishi and Niino*, 2009], and the Community Atmospheric Model shortwave and longwave radiation schemes [*Collins et al.*, 2004]. Note that we did not use the Yonsei University PBL scheme [*Hong et al.*, 2006], which was used in *F12*, except for in one of the sensitivity runs. The reason for this will be given in the next section.

Cumulus parameterization was switched off in both domains, as this is required for switching off latent heating in the microphysics scheme. However, we did perform one sensitivity run with the Grell-Freitas cumulus scheme [*Grell and Freitas*, 2014] enabled in both domains.

The sea ice extent and SST fields shown in Figure 1 were held fixed throughout all the model runs, which were all initialized at 12:00 UTC on 17 December 2002. (Note that from now on we will abbreviate times as the day of the month in December 2002 and the UTC time, e.g., 17/12 for the model initial time.) As

mentioned, the model runs in *F12* were initialized 12 h earlier, but we found that 17/12 gave more realistic results.

The bulk of our analysis is based on a number of sensitivity runs, in which we switched off latent heat release in the microphysics scheme, or surface heat fluxes, at different times. Up until those times, the sensitivity runs were identical to the control run, and we used the *restart* functionality to change the model setup.

In *F12*, version 2.2.1 of the WRF was used, and the code had been modified manually in order to inhibit latent heat release in the atmosphere. In version 3.0 this functionality was introduced as part of the official code (through the switch *no_mp_heating* in the namelist). What is actually done is that the temperature tendency is set to zero in the microphysics parameterization scheme. No other microphysical processes are affected.

2.2. Spectral Nudging

It has been shown that spectral nudging successfully inhibits variability in an ensemble of case simulations of a polar low even after 14 days of simulation time [*Zahn et al.*, 2008], clearly indicating that spectral nudging provides a way to deal with intraensemble variability due to differences in initial conditions. Keeping a more-or-less consistent storm track across multiple sensitivity studies of the polar low is important to make sure that the simulated lows develop in approximately the same location and are therefore driven by the same surface and large-scale atmospheric conditions. According to *F12*, upper level forcing played a role in the polar low development, as it generally does for polar lows [*Shapiro et al.*, 1987; *Montgomery and Farrell*, 1992; *Grønås and Kvamstø*, 1995; *Kolstad*, 2011; *Shimada et al.*, 2014]. As this forcing entered all our simulations via spectral nudging, the number of sources from which different results may emerge was reduced.

There are two potential concerns associated with nudging. First, latent heat release can affect upper level vorticity and it is therefore possible that the nudging dampens out some of the sensitivity to latent heating. However, we restricted the nudging to the outer 15 km domain and toward larger spatial scales (wind and temperature features with a wavelength of more than 730 km) above about 700 hPa.

Second, strong nudging may prohibit the development of extremes, in general, such as in tropical cyclones [*Cha et al.*, 2011], but several studies have shown that as long as the nudging is done carefully, extremes are not inhibited [*Colin et al.*, 2010; *Otte et al.*, 2012; *Glisan et al.*, 2013]. As mentioned, we used a weak form of nudging; the inner 3 km domain was only nudged indirectly through what was passed on at its boundary with the outer domain. We used WRF's default nudging strength, and nudging was switched off below model level 24 (about 700 hPa) and increased linearly to full strength on model level 29 (about 500 hPa). This means that the upper level large-scale conditions from the driving data were imposed on the simulations, while at the same time, the model was free to develop its own features at smaller scales between the surface up to the 700 hPa level, i.e., at the levels where the surface fluxes have the largest impact.

2.3. Data for Validation

It is difficult to evaluate the model runs because no direct observations exist. We therefore compared brightness temperatures and near-surface wind speeds from the model runs with advanced very high resolution radiometer (AVHRR) infrared satellite imagery and QuikSCAT scatterometer-derived wind speeds [*Hoffman and Leidner*, 2005], respectively. The computations of brightness temperatures and sea level pressure (SLP), as well as interpolations to pressure levels from the raw WRF data on model levels, were done using National Centers for Environmental Prediction's Unified Post Processor software (version 2.2).

2.4. Metrics

We computed some metrics as maximum values inside a circular region R, with a radius of 200 km, centered on the grid point with the lowest SLP value every hour.

We follow *Evans and Hart* [2003] and define a thermal wind based measure of cyclone structure as

$$-\mathrm{V}_T^L \stackrel{\mathrm{def}}{=\!=} \left.\frac{\partial(Z_{\mathrm{MAX}} - Z_{\mathrm{MIN}})}{\partial \ln p}\right|_{925\ \mathrm{hPa}}^{700\ \mathrm{hPa}},$$

where Z_{MAX} and Z_{MIN} are the maximum and minimum values, respectively, of geopotential height inside R at the specified pressure levels. Positive values of $-\mathrm{V}_T^L$ indicate a warm-core system with strong surface winds (since the thermal wind is antiparallel to the actual wind, which implies a negative wind shear with height).

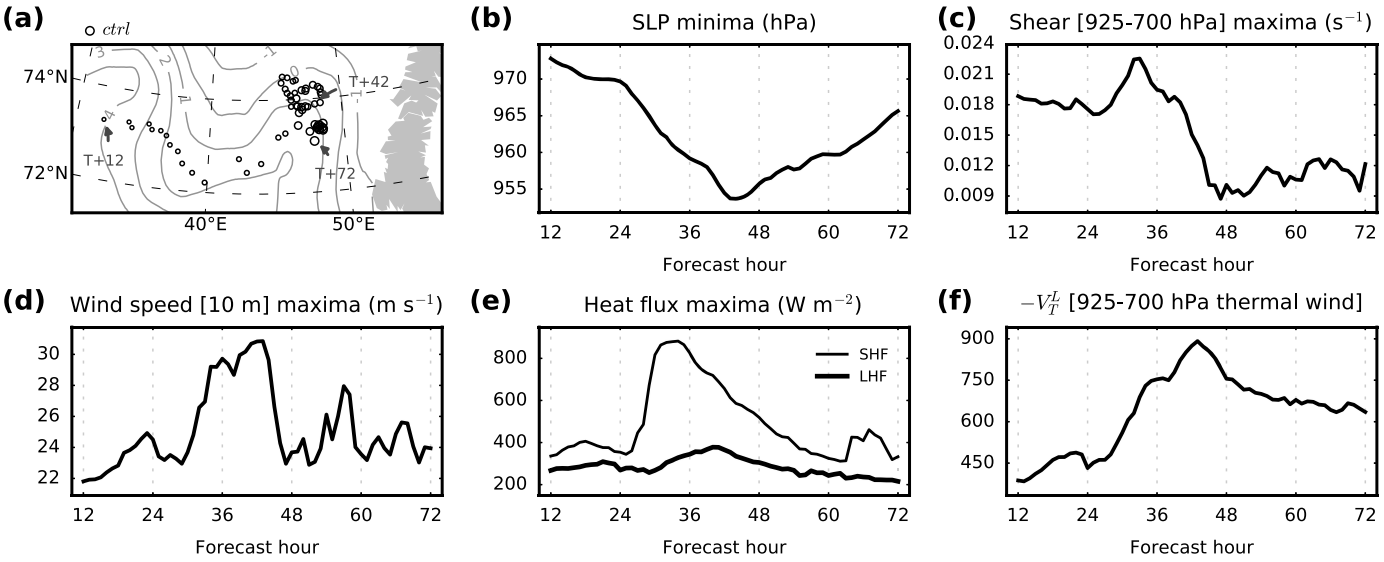

Figure 2. Hourly diagnostics for the control run. (a) The location of the lowest SLP value for each hour is shown, with circle sizes increasing with the forecast hour. The contours show the SSTs in °C. The rest of the panels show hourly values of (b) the SLP minima, (c) the maximum vertical wind shear inside a circular region *R* with a radius of 200 km around the low center, (d) the maximum 10 m wind speed inside *R*, (e) the maximum heat fluxes inside *R*, and (f) the warm-core indicator inside *R*.

The vertical wind shear was computed as

$$\left[\left(\frac{\partial u}{dz}\right)^2 + \left(\frac{\partial v}{dz}\right)^2\right]^{1/2}.$$

where *u* and *v* are the zonal and meridional wind components, respectively.

3. Results

3.1. The Control Run

Figure 2a shows the track of the polar low in the control run, and Figure 2b shows the evolution of the SLP minima. The minimum SLP (954 hPa) occurred about 42 h into the simulation (or in abbreviated form: $T+42$), i.e., at 19/06. This agrees with the polar low in *F12*, which peaked at 19/06, but their data were only shown for every 3 h. The storm track shows that the polar low did not make landfall in the simulation period (which ended at $T+72$, i.e., 20/12), whereas the polar low in the control run in *F12* made landfall at 20/12, too early when comparing with satellite imagery of the actual polar low.

The vertical wind shear in Figure 2c is the 95th percentile of the shear within 200 km from the low center at each time. As the graph shows that the polar low became equivalent barotropic at about $T+48$, it seems reasonable to refer to the period after $T+48$ as the mature phase of the polar low. The wind speed peaked around $T+42$, with maximum wind speeds near the low center almost reaching hurricane force (Figure 2d). The period of strong winds also coincided with the largest surface fluxes, with maximum sensible heat fluxes peaking around the time of maximum wind shear, and latent heat fluxes peaking around $T+42$ (Figure 2e). The likely reason for the peak in the wind speed is that the polar low developed a strong warm core between 925 and 700 hPa (Figure 2f) leading up to $T+42$. The thermal wind equation dictates that warm-core systems have strong surface winds.

In Figure 3, AVHRR satellite images taken at 3 times are shown along with brightness temperatures and SLP from the control run. Note that we do not know exactly how well the gray scale range that we chose for the top row corresponds to the images in the bottom row. In addition, the images in the bottom row were rotated and cropped manually to correspond as closely as possible with the projection in the top row. But in any case the white shades indicate low temperatures at the cloud tops and therefore deep convection.

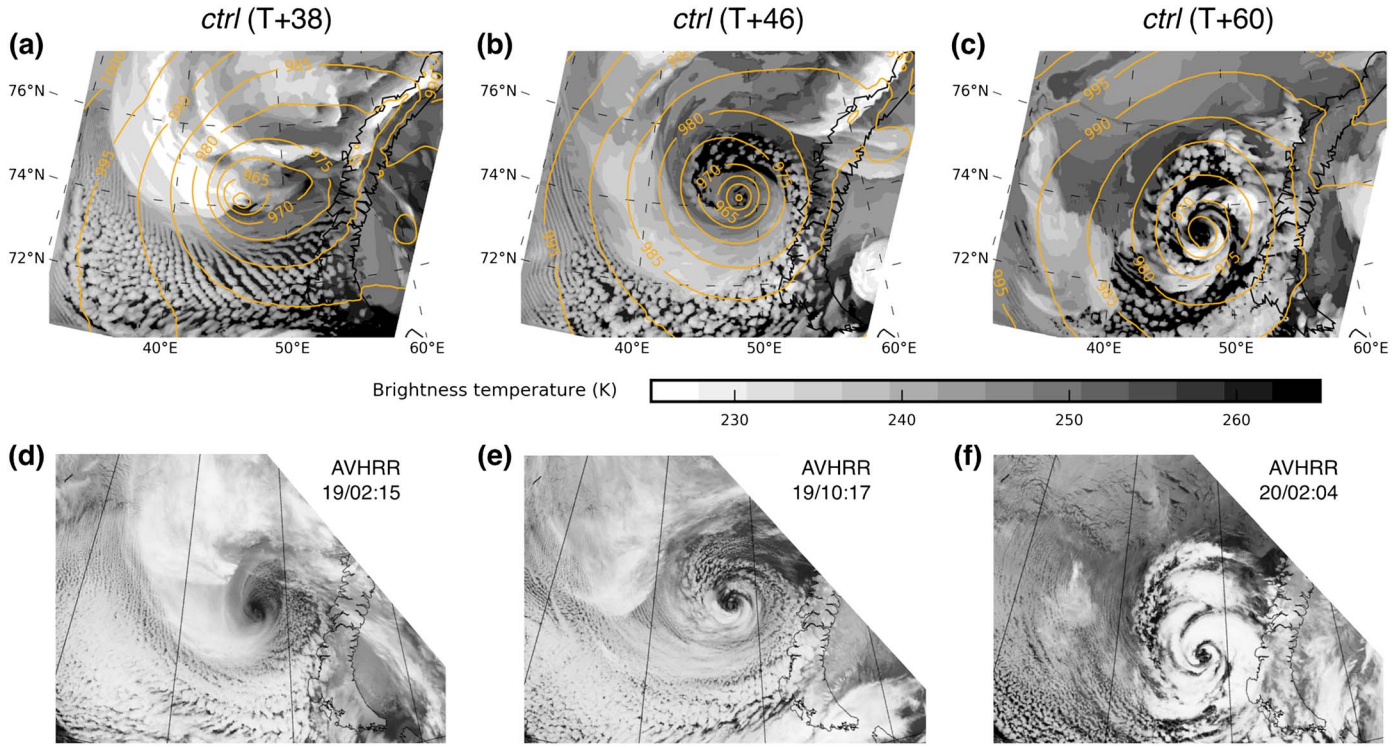

Figure 3. Brightness temperatures (gray scales) and SLP (colored contours every 5 hPa) from the control run *ctrl* at (a) 19/02, (b) 19/10, and (c) 20/02 (upper row) and (d–f) AVHRR channel 4 images taken at about the same times (lower row). The AVHRR images are reproduced with the kind permission of the Dundee Satellite Receiving Station in the U.K.

At the first time shown (Figure 3a), the simulated low was positioned slightly west of the actual low (Figure 3d), and the simulated convection appears to be less vigorous than in reality. The next time shown is 19/10, just after the peak of the simulated development. As shown later, the wind speeds in the simulation had dropped substantially by then. The position of the low at this time was very accurate (Figures 3b and 3e). Later on, at 20/02, the position of the simulated low still agreed with the satellite image, and the cloud structures look similar, although the patches of high and white cloud tops near the eye seem to have been larger in reality than in the simulations (Figures 3c and 3f). This probably indicates that the model underestimated the depth of the convection.

In Figures 4a–4c, snapshots of SLP and geopotential height at 500 hPa in *ctrl* are shown for the same times as the brightness temperatures in Figure 3. These confirm the equivalent barotropic state following the peak of the polar low. Note also how the lows both aloft and at the surface had deepened between $T+38$ and $T+46$ and declined in intensity between $T+46$ and $T+60$. Figures 4d–4f show the low-level temperature for the same times as those shown in Figures 4a–4c. The first of these (Figure 4d) shows an occluded front, and by the next time a warm core had formed (Figure 4e). Later on, in the maintenance phase, the system still had a warm core (Figure 4f), but by this time the whole southern region had warmed up considerably due mainly to surface heat fluxes, as shown later.

Figure 5 shows a comparison of wind speed percentiles from QuikSCAT and the control run. At the first time shown ($T+32$), the QuikSCAT wind speeds were higher than the ones from the model, but only 4 h later ($T+36$, 6 h before the peak in wind speed in the control run), the opposite situation occurred. For the latter 2 times shown, during the mature stage of the control run polar low, the wind speeds from QuikSCAT and the control run were more in agreement, but with QuikSCAT yielding overall stronger winds. It is difficult to assess the accuracy of the control simulation based only on QuikSCAT imagery.

In summary, based on our qualitative comparison with satellite imagery, we conclude that the simulated low gave a good reproduction of the position, cloud structure, and near-surface wind speeds of the actual polar low, especially after the polar low had reached its mature stage.

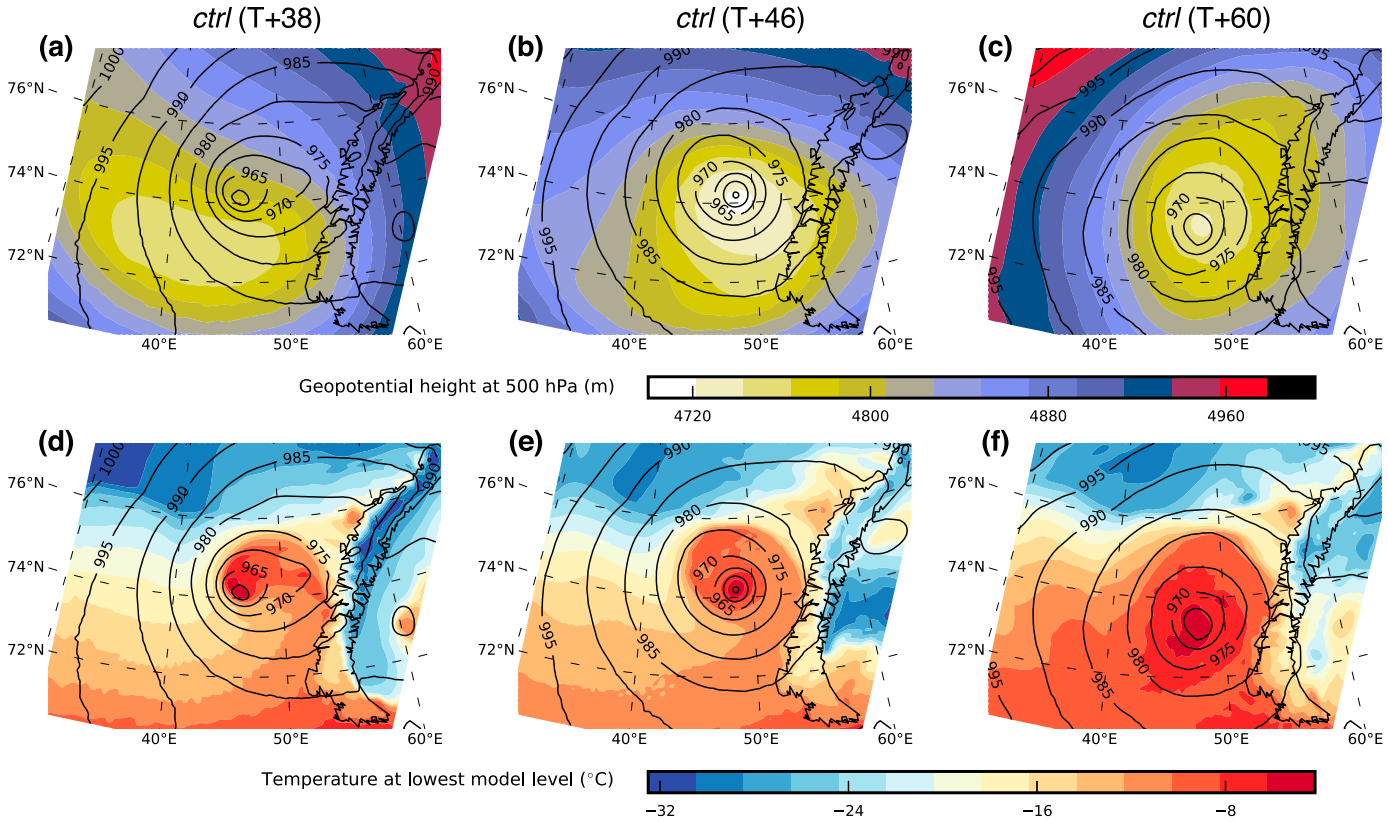

Figure 4. Geopotential height at 500 hPa (colors) and SLP (black contours every 5 hPa) from the control run at (a) 19/02, (b) 19/10, and (c) 20/02, and (d–f) temperature at the lowest model level (colors) and SLP for the same times.

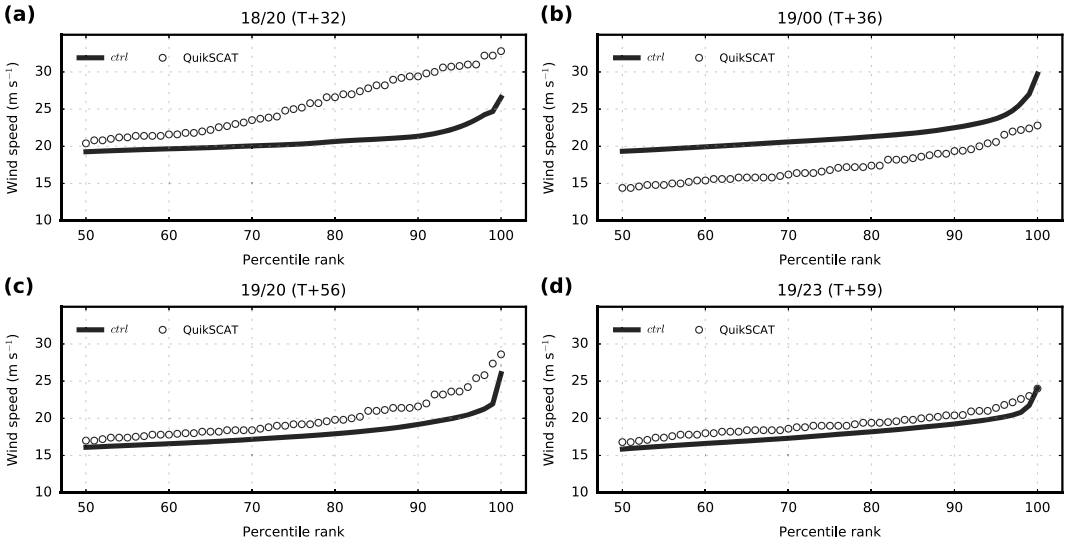

Figure 5. Comparison between QuikSCAT wind speeds and WRF 10 m wind speeds in the control run at four different times. Note that the timing of the QuikSCAT observations is not unequivocal, as each frame was constructed from several passes. The curves and circles show the percentiles of wind speed inside circular region with radii of 200 km, centered on the cores of the polar lows at each time and for each experiment. The centers of the regions were determined by the minimum QuikSCAT wind speeds in the vicinity of the low centers in the control run.

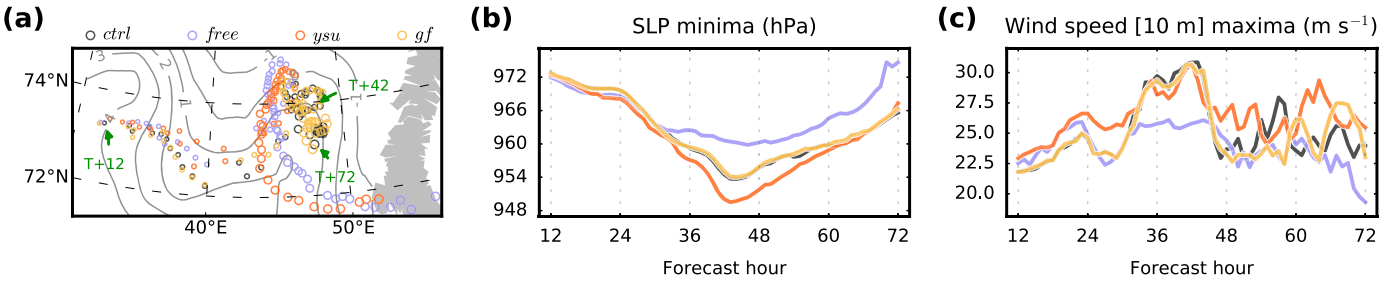

Figure 6. Hourly diagnostics for the *ctrl*, *free*, *ysu*, and *gf* model runs. (a) The location of the lowest SLP value for each hour is shown, with circle sizes increasing with the forecast hour and circle colors indicating the model run. The contours show the SSTs in °C. The rest of the panels show hourly values of (b) the SLP minima and (c) the maximum 10 meter wind speed inside a circular region with a radius of 200 km around the low center, following the color scheme in Figure 6a.

3.2. The Effects of Nudging and Parameterization

We now demonstrate that nudging was crucial for reproducing the evolution of this particular polar low. We also show that cumulus parameterization had almost no effect on the simulation of the polar low, but that the PBL scheme used in *F12* gave very different results to the ones for our control run.

Figure 6a shows the tracks of the control run and three model runs that were identical to the control run except: nudging was switched off in the model run labeled *free*, the Grell-Freitas cumulus scheme was used in both domains in *gf*, and the Yonsei University PBL scheme was used in *ysu*. The tracks were identified through an objective identification of the hourly minima in SLP for all the open-ocean grid points inside the domain.

The incipient simulated polar lows in the *free* and *ysu* model runs initially moved eastward along a trajectory slightly farther north than in the control run (Figure 6a). At about $T+24$, the polar low in *ctrl* migrated north-east and then moved around in three loops. The *ysu* and *free* lows also moved north, but farther to the west than the control run, and then they curved far toward the south-east. Note that the control run polar low in *F12*, where the Yonsei University PBL scheme was used, also moved in one wide loop, much in the same way as the low in our *ysu* experiment. Images of brightness temperatures for the *free* and *ysu* runs make it clear that the evolutions of the polar lows in those two runs deviated significantly from what actually happened (not shown). Figures 6b and 6c show that the *free* run did not produce the defined minimum in SLP and the peak in wind speed found in the control run, although the magnitude of the fluxes was comparable (not shown). It also yielded lower $-V_T^L$ values than the control run (not shown). Figure 6b shows that the *ysu* polar low was deeper than the one in the control run, reaching just below 950 hPa. The *ysu* run produced very high wind speeds (Figure 6c) and extremely strong heat fluxes (not shown). The latent heat fluxes were in agreement with those found in *F12* (about 400 W m^{-2}), but the *F12* control run had sensible heat fluxes of about 1200 W m^{-2} close to the low center, well below the values in our *ysu* run. The maximum sensible heat flux in the *ysu* run was 2150 W m^{-2}. This is substantially higher than the sensible heat fluxes in our control run and also much higher than the fluxes in *F12*. The high, and probably unrealistic, fluxes could be the reason for the lower SLP minima found in the *ysu* run.

Piqued by the similarities between the storm tracks of the *ysu* and *free* runs, we also performed a variant of the *ysu* run with considerably stronger nudging. This led to a track that was closer to the one in the control run, but the heat fluxes were still much larger than the ones in the control run, and the SLP minimum was identical to the one in the *ysu* experiment. This indicates that it was differences in the PBL schemes (and not the diverging storm track) that led to the discrepancies between *ysu* and *ctrl*.

The behavior of the polar low in the *gf* model run was virtually indistinguishable from the one in *ctrl* (Figure 6). This suggests that cumulus parameterization had little effect in this case; this could be because the Grell-Freitas cumulus scheme is scale-dependent and adapts to the horizontal resolution [*Arakawa et al.*, 2011]. As the 3 km inner domain was able to resolve the larger convective cells, the effect of the cumulus scheme was probably smaller than it would have been at coarser resolutions.

3.3. Impacts of Fluxes and Latent Heating

Our main analysis is focused on sensitivity runs where heating and fluxes were switched off at $T+30$, when the polar low in the control run was located just east of 40°E and had started to move toward the northeast

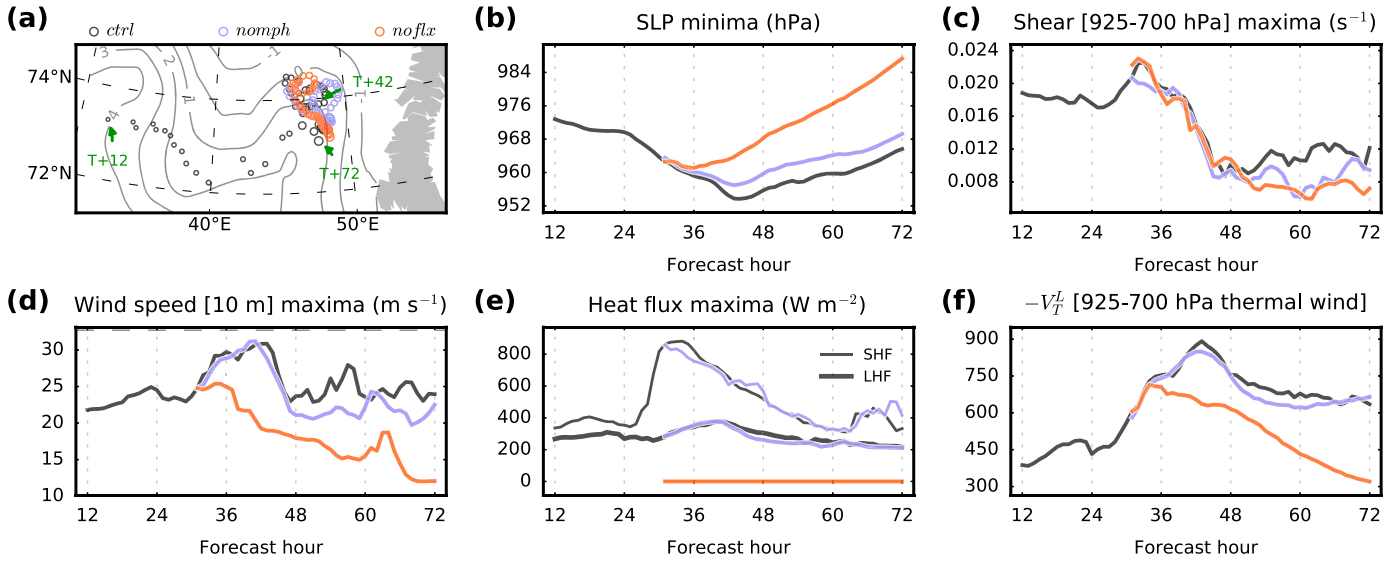

Figure 7. Hourly diagnostics for the control run and the sensitivity runs where heating, fluxes, and both were switched off at $T+30$. (a) The location of the lowest SLP value for each hour is shown, with circle sizes increasing with the forecast hour and circle colors indicating the model run. The contours show the SSTs in °C. The rest of the panels show hourly values of (b) the SLP minima, (c) the maximum vertical wind shear inside a circular region R with a radius of 200 km around the low center, (d) the maximum 10 meter wind speed inside R , (e) the maximum heat fluxes inside R, and (f) the warm-core indicator inside R, following the color scheme in Figure 7a.

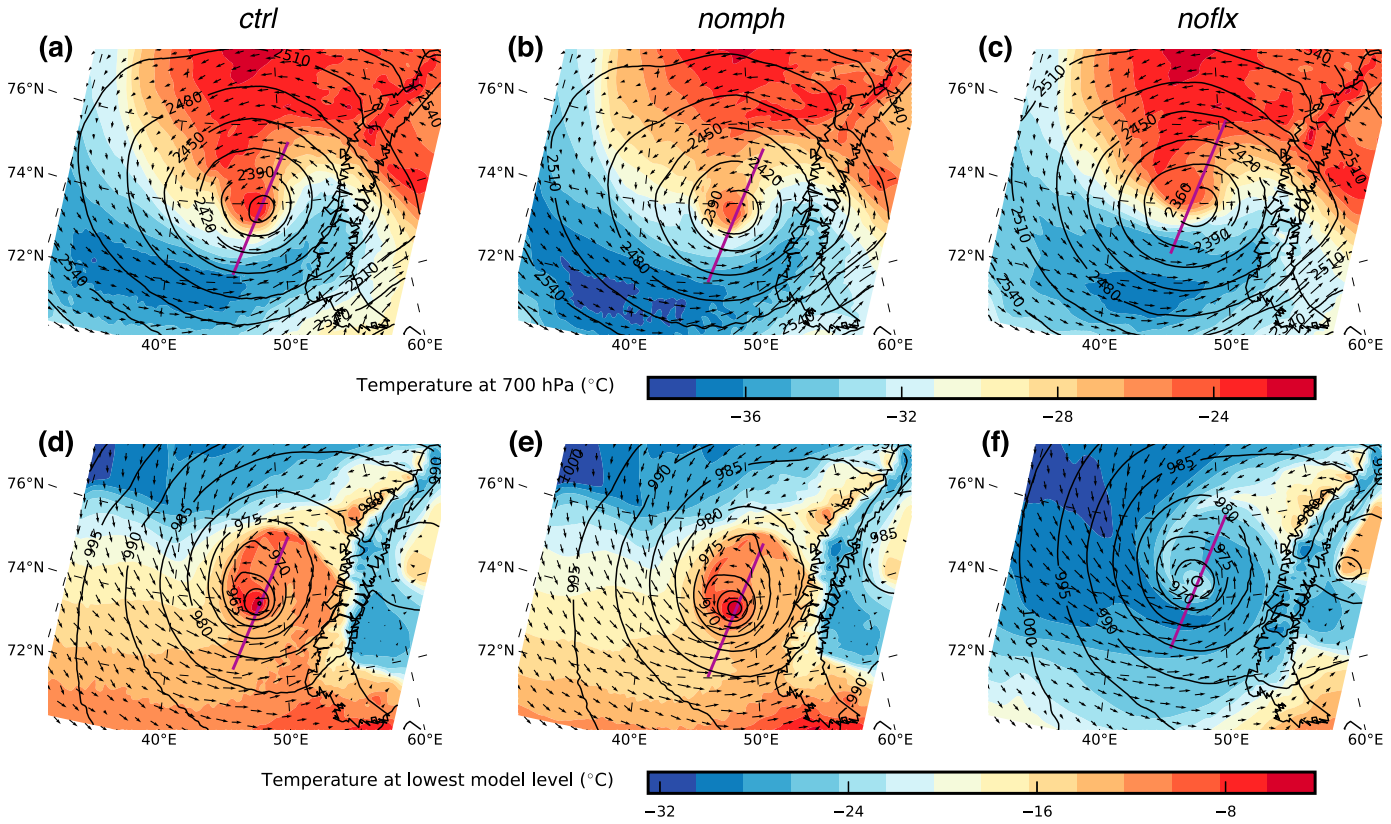

Figure 8. Temperature and flow variables at $T+42$ for the *ctrl*, *nomph*, and *noflx* model runs. (a–c) Temperature (colors), geopotential height (contours), and wind vectors (arrows) at 700 hPa are shown. (d–f) Temperature (colors) and wind vectors (arrows) at the lowest model level are shown along with SLP (contours). The purple lines indicate the lower boundary of the vertical cross sections in Figure 10.

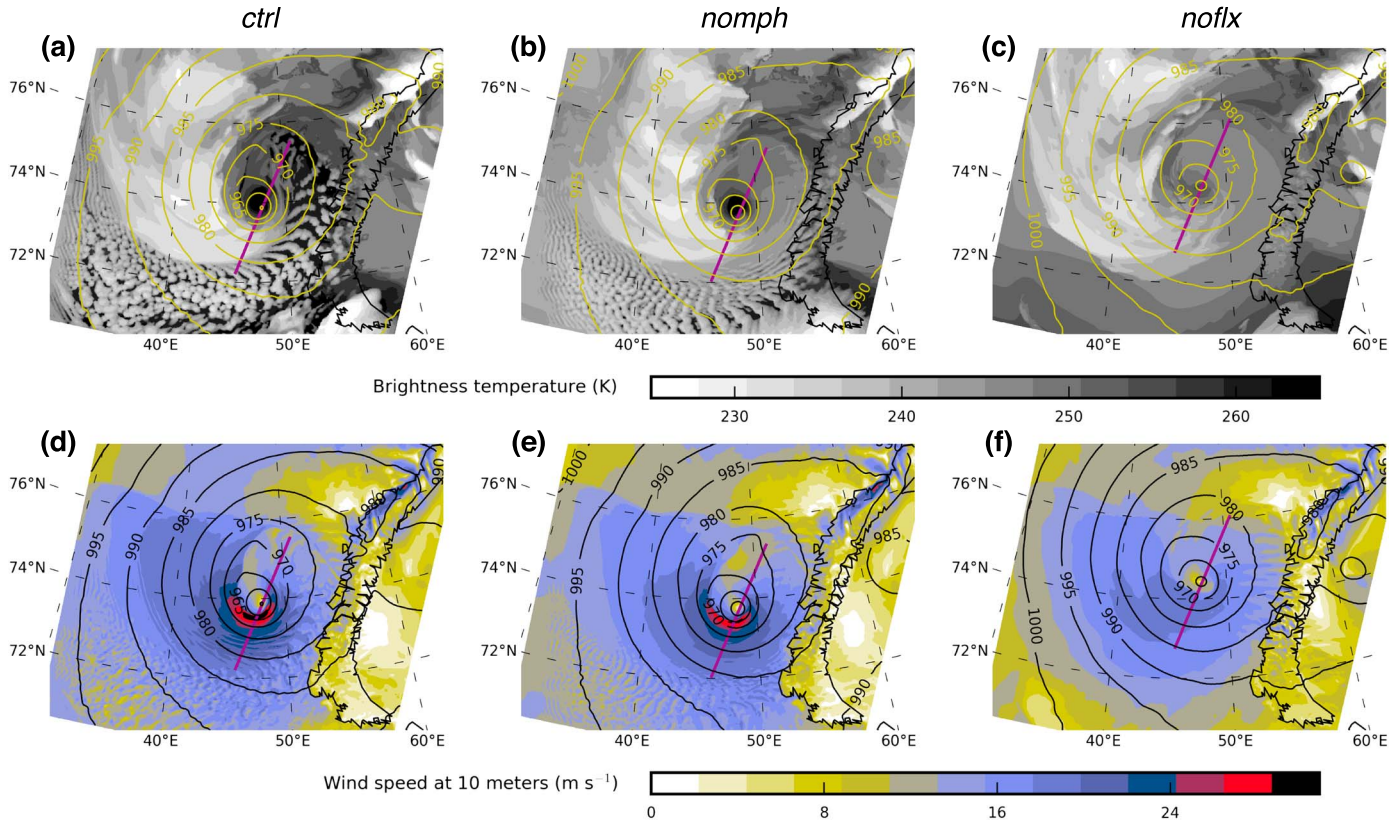

Figure 9. Brightness temperatures and wind speed at $T+42$ for the *ctrl*, *nomph*, and *noflx* model runs. (a–c) Brightness temperatures (gray scales) and SLP (contours) are shown. (d–f) Wind speed (colors) is shown along with SLP (contours). The purple lines indicate the lower boundary of the vertical cross sections in Figure 10.

(Figure 7a). The SLP at that time was decreasing rapidly from a plateau at about 970 hPa (Figure 7b). With surface fluxes switched off but latent heating active (*noflx*), the SLP continued to drop until about $T+36$, but after that the pressure started to increase at a steeper rate than in the control run. The experiment with no latent heating but with active fluxes behaved more similarly to the control run, although its simulated SLP values were not as low (Figure 7b). The wind shear, i.e., baroclinicity, followed similar evolutions in all three runs (Figure 7c).

The *nomph* run produced similar near-surface wind speeds (Figure 7d) and surface fluxes (Figure 7e) as the control run. The warm core dissipated more rapidly in the *noflx* experiment than in *nomph* and *ctrl* (Figure 7f), and as a consequence, the near-surface wind speed also decayed rapidly (Figure 7d).

Figure 8 shows temperatures both at 700 hPa and at the lowest model level (about 17 m) at $T+42$. Near the surface, the warm air being advected into the low center in *ctrl* originated from the Barents Sea and was channeled northward and contained by the barrier of Novaya Zemlya (Figure 8d). The lack of surface fluxes in *noflx* meant that the polar low had less access to warm air than *ctrl* and *nomph*, and as a consequence the low-level temperatures in *noflx* (Figure 8f) were lower than in the other two model runs (Figures 8d and 8e). In the Kara Sea, east of Novaya Zemlya, the ocean was covered by sea ice, so that the *noflx* experiment was slightly warmer than the other two experiments because the air was not cooled from below. This favored warm advection from the east into the core aloft and contributed to the maintenance of the low pressure at 700 hPa in *noflx*. In addition, all the simulations were constrained by the spectral nudging from 700 hPa and upward.

Figure 9 shows brightness temperatures and wind speeds for the experiments at $T+42$ (19/06), the time of the peak in wind speeds in the control run. Figure 9a shows that the control run produced vigorous convection cells in the southern part of the region. Some, but less distinct, organized low-level convection also occurred in *nomph* (Figure 9b), whereas the *noflx* experiment seems to have had no convection cells (Figure 9c). It was mainly near the core of the polar low that the near-surface wind speeds were substantially higher in *ctrl* (Figure 9d) and *nomph* (Figure 9e) than in *noflx* (Figure 9f). These high near-surface wind speeds

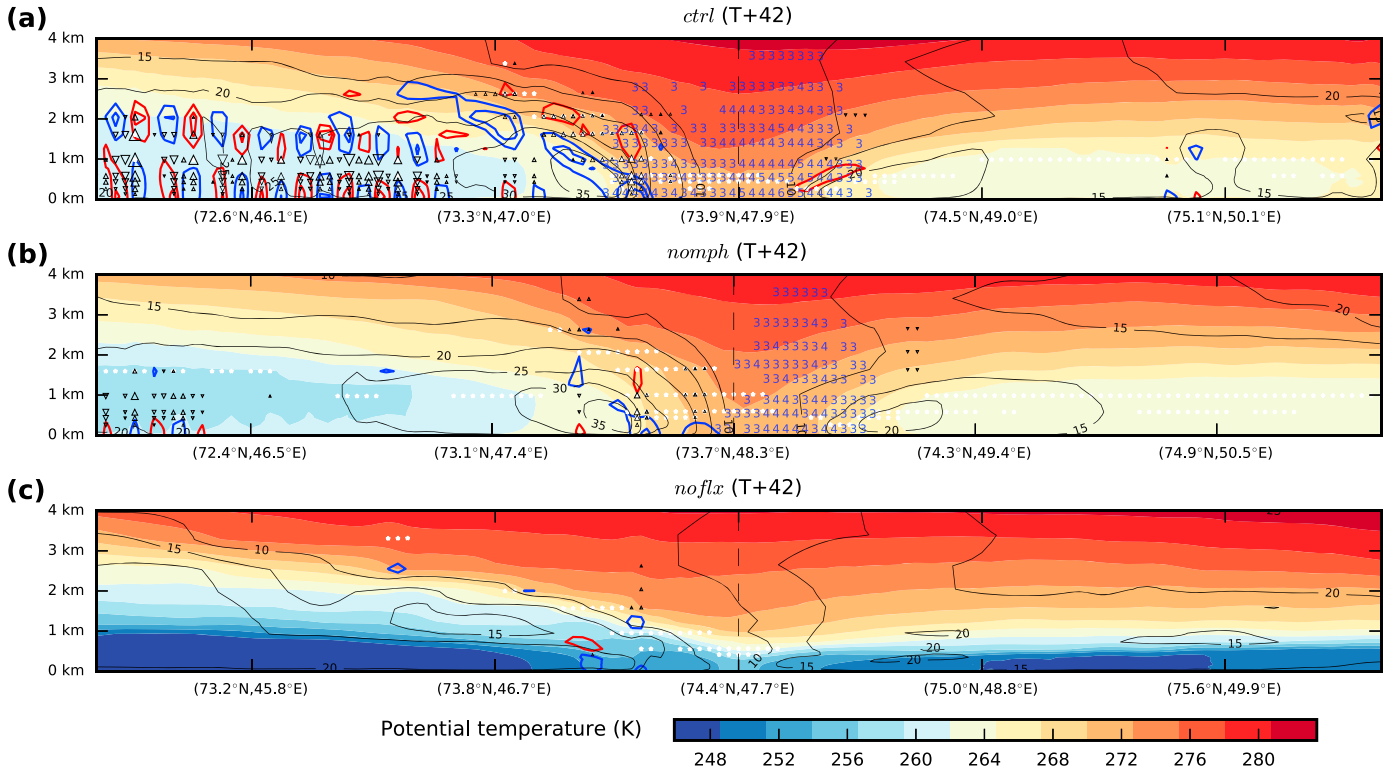

Figure 10. Vertical cross sections above the purple lines shown in Figures 8 and 9. The colors show potential temperature; the triangles show vertical wind speeds (ω) above 3 hPa s^{-1}, scaled according to the magnitude and with the direction of motion indicated by the triangles; the white asterisks show points with relative humidity > =95%; the black contours show horizontal wind speed in m s^{-1}; the blue (negative values) and red (positive values) contours show divergence with an interval of 4×10^{-4} s^{-1}; and the blue numbers indicate the local decrease in pressure in hPa over the previous hour.

coincide with local maxima of heat fluxes in *ctrl* and *nomph* (not shown), which indicates that the warm-core structure was instrumental in producing the strong winds. It also suggests that it was surface heat fluxes and the wrapping around of the warm air into the low center at low levels that generated the strong winds, rather than latent heat release. In fact, the similarities between the polar lows in the *ctrl* and *nomph* experiments indicate that latent heating had a negligible effect in strengthening the polar low at low levels.

The vertical cross sections in Figure 10 were selected so that they intersected the low centers and the region with the maximum 10 m wind speed in the control run, and their locations are indicated with purple lines in Figures 8 and 9. The differences between the control run (Figure 10a) and the *nomph* experiment (Figure 10b) were mainly as follows: (1) The *ctrl* run produced convective cells in the left part of the picture (south-southwest of the low center), with fairly evenly spaced updraft and downdraft regions. (2) Latent heating above 1 km along the front just to the left of the low center in the control run gave stronger convection and divergence aloft and convergence below, driving the pressure down locally. This pattern was less pronounced in *nopmph*, where upward and downward motions was generally weaker. The polar low in the *noflx* experiment (Figure 10c) did not intensify and had a less clearly defined warm core and lower temperatures at low levels than the lows in the other two runs.

4. Discussion

This paper assessed the roles of latent heat release and surface fluxes in the life cycle of an intense and unusually long-lasting polar low. Spectral nudging was used to maintain consistent large-scale conditions across the different sensitivity tests. This polar low is of particular interest due to its "hurricane-like" cloud structure evident in its later stages (see Figures 3e and 3f). A key question is the extent to which intensification occurred during this period and in addition whether the driving mechanisms were indeed consistent with hurricane intensification, or if the polar low was a "normal" extratropical marine cyclone.

A previous study of the polar low studied here was affected by considerable differences between the simulated tracks in their sensitivity experiments [*Føre et al.*, 2012; *F12*]. These differences hindered interpretation, particularly with regard to the mature stage of the polar low. Here results are presented with the polar low track more tightly constrained across different experiments, which was achieved by using spectral nudging toward the large-scale flow in the vicinity of the polar low in contrast to the *F12* study, where the low was allowed to evolve freely in the inner model domain constrained only at the outer boundaries. To our knowledge, no previous model-based polar low case studies have employed spectral nudging. We believe that our approach could and should be used in future case studies of polar lows and other cyclones where small changes to the state of the cyclone can lead to large deviations of the storm track.

Our simulations indicate a period of baroclinic growth up until approximately 19/06 (i.e., 06:00 UTC on 19 December 2002). Around that time both the pressure and the wind speeds plateaued and started to increase and decrease, respectively. This was also when the low centers at the surface and at 500 hPa became in phase, and the system became equivalent barotropic. What followed then was a period of more than 24 h with slowly increasing pressure and maintenance of maximum near-surface wind speeds of almost 25 ms^{-1}. Surface fluxes were almost entirely responsible for maintaining the intensity of the polar low during the mature phase. Figures 7–10 show that this maintenance was achieved through the maintenance of a deep warm core and that this did not occur in the sensitivity experiment where surface fluxes were switched off. The surface fluxes were extremely large because the polar low occurred in an unusually strong cold air outbreak.

Because there are numerous types of polar lows, from comma clouds to hurricane-like systems, and because individual polar lows can go through several phases, it is difficult to draw a clear line between normal marine cyclones and polar lows. For instance, the following similarities between explosive marine cyclones [*Sanders and Gyakum*, 1980; *Gyakum et al.*, 1992; *Allen et al.*, 2010] near Iceland and Greenland and polar lows were highlighted by *Wang and Rogers* [2001]: "a short life cycle, strong low-level baroclinicity, and weak stability in the vertical, and their developments, are both initiated by an upper level cyclonic vorticity advection (or potential vorticity anomaly) under northerly winds."

The following factors separated the polar low studied here from a regular marine cyclone: (1) The polar low formed in an extreme cold air outbreak close to the sea ice edge and in a region with low SSTs far away from the main polar front. (2) The surface fluxes were unusually high (Figure 2e) and contributed to the maintenance of a warm core (Figure 2f) and strong surface winds (Figure 2d) long after the end of the baroclinic phase of the system (Figure 2c).

Although the results presented here are qualitatively similar to *F12*, a major difference is that the polar low became much more intense in the nudged control simulation, with a minimum pressure of 954 hPa here compared to 961 hPa for the unnudged control run in *F12*, despite about 1.5 times higher sensible heat fluxes in *F12* than in our experiments. (Note that our *ysu* sensitivity run, using the YSU PBL scheme used in *F12*, produced an even deeper low: 950 hPa.) This difference is probably associated with the implementation of spectral nudging, since the unnudged simulation conducted here was found to give a very similar minimum SLP to that seen in *F12* (Figure 6). The likely explanation for this is that the track in the unnudged simulation passed over regions of lower sea surface temperatures and therefore incurred less surface heating.

Another key difference with respect to *F12* is that turning off latent heating resulted in a more intense polar low during the mature phase in *F12*. This unexpected result was not reproduced in the nudged sensitivity studies described here. This indicates that the impacts of latent heat release have been more reliably identified without the confounding impact of large deviations in the polar low track and large-scale structure. But to first order, our conclusions about the mechanisms that were instrumental in the development and maintenance of the polar low match those of *F12*. After the baroclinic intensification stage, which culminated with a deep warm core and a maximum in surface wind speeds, strong surface fluxes (in combination with upper level forcing) drove the maintenance of the warm core, thus giving an extended and strong maintenance phase.

Our case stands out somewhat compared to previous numerical experiments, which have generally found that switching off surface fluxes and/or latent heating resulted in a much weaker polar low [*Albright et al.*, 1995; *Blier*, 1996; *Mailhot et al.*, 1996; *Bresch et al.*, 1997]. We found that latent heating played a minor role compared to surface heat fluxes. The most likely reason for the difference is that latent heating and fluxes were turned off at or before the incipient stage of the polar low development in the previous studies,

whereas our sensitivity tests involved turning off fluxes/heating when the polar low was already well developed.

Although hurricane-like intensification is theoretically possible in arctic conditions, it appears that even in this case, with strong winds and high surface fluxes, further intensification did not occur during the hurricane-like later stages of the development. But it is possible that the fluxes were not quite strong enough. Figure 2 showed the sensible and latent heat fluxes near the surface low center throughout the control run. The total heat fluxes peaked around $T+33$ at slightly over 1100 Wm^{-2} and declined along with the wind speed after the peak at $T+42$. At $T+51$ the total fluxes were about 700 Wm^{-2} and were stably in the range 500–600 Wm^{-2} from $T+56$ and onward. As shown by *Albright et al.* [1995], drastic, and probably unrealistic, SST increases (8 K in their case), can tip a hurricane-like polar low, i.e., a barotropic system maintained by surface fluxes like the one studied here, into a system that exhibits growth in what would normally be the maintenance stage. For future work, we propose to investigate the effects of an artificial SST increase on the low studied here and perhaps other hurricane-like polar lows over the Barents Sea.

The results of this study demonstrate that even in today's climate, near-hurricane force winds may occur during strong baroclinic developments in combination with large surface energy fluxes. The effects of climate change on polar lows are likely to be complex due to the many processes that affect their intensification, duration, and decay. For example, in addition to the projected poleward shift of polar low density as sea ice retreats in the future [*Kolstad and Bracegirdle*, 2008; *Zahn and von Storch*, 2010], larger areas of open ocean (i.e., with no sea ice) could result in longer lifetimes as larger expanses of open ocean and higher SSTs allow for more extended maintenance/decay phases. Note that a poleward shift also means a stronger Coriolis force, which may accelerate the intensification of polar lows. In summary, the northeast Barents Sea is likely to be a region of particularly significant change in polar low frequency and characteristics.

Acknowledgments

The authors would like to thank two anonymous reviewers for their efforts in improving the paper. We also thank the vast community that has developed and continues to maintain the WRF model, as well as the ECMWF for providing the ERA-Interim reanalysis data. E.W.K.'s work was funded by the Research Council of Norway through the Hordaklim project (project 245403). T.J.B. conducted this work as part of the British Antarctic Survey science program Polar Science for Planet Earth, which is funded by the Natural Environment Research Council. M.Z. was supported through the Cluster of Excellence "CliSAP" (EXC177), Universität Hamburg, 501 funded through the German Science Foundation (DFG). The data used can be made available on demand by contacting E.W.K. at erik.kolstad@uni.no.

References

Albright, M. D., R. J. Reed, and D. W. Ovens (1995), Origin and structure of a numerically simulated polar low over Hudson Bay, *Tellus*, *47A*(5), 834–848.

Allen, J. T., A. B. Pezza, and M. T. Black (2010), Explosive cyclogenesis: A global climatology comparing multiple reanalyses, *J. Clim.*, *23*(24), 6468–6484, doi:10.1175/2010JCLI3437.1.

Arakawa, A., J.-H. Jung, and C.-M. Wu (2011), Toward unification of the multiscale modeling of the atmosphere, *Atmos. Chem. Phys.*, *11*(8), 3731–3742.

Blechschmidt, A. M. (2008), A 2-year climatology of polar low events over the Nordic Seas from satellite remote sensing, *Geophys. Res. Lett.*, *35*, L09815, doi:10.1029/2008GL033706.

Blier, W. (1996), A numerical modeling investigation of a case of polar airstream cyclogenesis over the Gulf of Alaska, *Mon. Weather Rev.*, *124*(12), 2703–2725, doi:10.1175/1520-0493(1996)124<2703:ANMIOA>2.0.CO;2.

Bracegirdle, T. J., and D. B. Stephenson (2012), Higher precision estimates of regional polar warming by ensemble regression of climate model projections, *Clim. Dyn.*, *39*(12), 2805–2821, doi:10.1007/s00382-012-1330-3.

Bracegirdle, T. J., and S. L. Gray (2008), An objective climatology of the dynamical forcing of polar lows in the Nordic seas, *Int. J. Climatol.*, *28*(14), 1903–1919, doi:10.1002/joc.1686.

Bracegirdle, T. J., and S. L. Gray (2009), The dynamics of a polar low assessed using potential vorticity inversion, *Q. J. R. Meteorol. Soc.*, *135*(641), 880–893.

Bresch, J. F., R. J. Reed, and M. D. Albright (1997), A polar-low development over the Bering Sea: Analysis, numerical simulation, and sensitivity experiments, *Mon. Weather Rev.*, *125*(12), 3109–3130.

Cha, D. H., C. S. Jin, D. K. Lee, and Y. H. Kuo (2011), Impact of intermittent spectral nudging on regional climate simulation using Weather Research and Forecasting model, *J. Geophys. Res.*, *116*, D10103, doi:10.1029/2010JD015069.

Chen, F., H. von Storch, L. Zeng, and Y. Du (2014), Polar low genesis over the North Pacific under different global warming scenarios, *Clim. Dyn.*, *43*, 3449–3456, doi:10.1007/s00382-014-2117-5.

Colin, J., M. Déqué, R. Radu, and S. Somot (2010), Sensitivity study of heavy precipitation in Limited Area Model climate simulations: Influence of the size of the domain and the use of the spectral nudging technique, *Tellus A*, *62*(5), 591–604.

Collins, W. D., P. J. Rasch, B. A. Boville, J. J. Hack, J. R. McCaa, D. L. Williamson, J. T. Kiehl, B. Briegleb, C. Bitz, and S. Lin (2004), *Description of the NCAR Community Atmosphere Model (CAM 3.0)*, Natl. Cent. for Atmos. Res., Boulder, Colo.

Dee, D. P., et al. (2011), The ERA-Interim reanalysis: Configuration and performance of the data assimilation system, *Q. J. R. Meteorol. Soc.*, *137*(656), 553–597, doi:10.1002/qj.828.

Emanuel, K. A., and R. Rotunno (1989), Polar lows as arctic hurricanes, *Tellus*, *41A*(1), 1–17.

Ese, T., I. Kanestrøm, and K. Pedersen (1988), Climatology of polar lows over the Norwegian and Barents Seas, *Tellus*, *40A*(3), 248–255.

Evans, J. L., and R. E. Hart (2003), Objective indicators of the life cycle evolution of extratropical transition for Atlantic tropical cyclones, *Mon. Weather Rev.*, *131*(5), 909–925, doi:10.1175/1520-0493(2003)131<0909:OIOTLC>2.0.CO;2.

Fletcher, J., S. Mason, and C. Jakob (2016), The climatology, meteorology, and boundary layer structure of marine cold air outbreaks in both hemispheres, *J. Clim.*, *29*(6), 1999–2014, doi:10.1175/JCLI-D-15-0268.1.

Føre, I., J. E. Kristjánsson, E. W. Kolstad, T. J. Bracegirdle, Ø. Saetra, and B. Røsting (2012), A 'hurricane-like'polar low fuelled by sensible heat flux: High-resolution numerical simulations, *Q. J. R. Meteorol. Soc.*, *138*(666), 1308–1324.

Glisan, J. M., W. J. Gutowski Jr., J. J. Cassano, and M. E. Higgins (2013), Effects of spectral nudging in WRF on Arctic temperature and precipitation simulations, *J. Clim.*, *26*(12), 3985–3999.

Grell, G. A., and S. R. Freitas (2014), A scale and aerosol aware stochastic convective parameterization for weather and air quality modeling, *Atmos. Chem. Phys.*, *14*(10), 5233–5250, doi:10.5194/acp-14-5233-2014.
Grønås, S., and N. G. Kvamstø (1995), Numerical simulations of the synoptic conditions and development of Arctic outbreak polar lows, *Tellus*, *47A*(5), 797–814.
Gyakum, J. R., P. J. Roebber, and T. A. Bullock (1992), The role of antecedent surface vorticity development as a conditioning process in explosive cyclone intensification, *Mon. Weather Rev.*, *120*(8), 1465–1489, doi:10.1175/1520-0493(1992)120<1465:TROASV>2.0.CO;2.
Hoffman, R. N., and S. M. Leidner (2005), An introduction to the near-real-time QuikSCAT data, *Weather Forecasting*, *20*(4), 476–493, doi:10.1175/WAF841.1.
Hong, S.-Y., Y. Noh, and J. Dudhia (2006), A new vertical diffusion package with an explicit treatment of entrainment processes, *Mon. Weather Rev.*, *134*(9), 2318–2341.
Hoskins, B. J., and P. J. Valdes (1990), On the existence of storm-tracks, *J. Atmos. Sci.*, *47*(15), 1854–1864, doi:10.1175/1520-0469(1990)047<1854:OTEOST>2.0.CO;2.
Koenigk, T., R. Döscher, and G. Nikulin (2011), Arctic future scenario experiments with a coupled regional climate model, *Tellus A*, *63*(1), 69–86, doi:10.1111/j.1600-0870.2010.00474.x.
Koenigk, T., L. Brodeau, R. Graversen, J. Karlsson, G. Svensson, M. Tjernström, U. Willén, and K. Wyser (2013), Arctic climate change in 21st century CMIP5 simulations with EC-Earth, *Clim. Dyn.*, *40*(11-12), 2719–2743, doi:10.1007/s00382-012-1505-y.
Kolstad, E. W. (2011), A global climatology of favourable conditions for polar lows, *Q. J. R. Meteorol. Soc.*, *137*(660), 1749–1761, doi:10.1002/qj.888.
Kolstad, E. W. (2015), Extreme small-scale wind episodes over the Barents Sea: When, where and why?, *Clim. Dyn.*, *45*(7), 2137–2150, doi:10.1007/s00382-014-2462-4.
Kolstad, E. W., and T. J. Bracegirdle (2008), Marine cold-air outbreaks in the future: An assessment of IPCC AR4 model results for the Northern Hemisphere, *Clim. Dyn.*, *30*(7–8), 871–885, doi:10.1007/S00382-007-0331-0.
Kolstad, E. W., T. J. Bracegirdle, and I. A. Seierstad (2009), Marine cold-air outbreaks in the North Atlantic: Temporal distribution and associations with large-scale atmospheric circulation, *Clim. Dyn.*, *33*(2), 187–197, doi:10.1007/s00382-008-0431-5.
Lindzen, R. S., and B. Farrell (1980), A simple approximate result for the maximum growth rate of baroclinic instabilities, *J. Atmos. Sci.*, *37*(7), 1648–1654.
Mailhot, J., D. Hanley, B. Bilodeau, and O. Hertzman (1996), A numerical case study of a polar low in the Labrador Sea, *Tellus*, *48A*(3), 383–402.
Miguez-Macho, G., G. L. Stenchikov, and A. Robock (2004), Spectral nudging to eliminate the effects of domain position and geometry in regional climate model simulations, *J. Geophys. Res.*, *109*, D13104, doi:10.1029/2003JD004495.
Montgomery, M. T., and B. F. Farrell (1992), Polar low dynamics, *J. Atmos. Sci.*, *49*(24), 2484–2505.
Nakanishi, M., and H. Niino (2009), Development of an improved turbulence closure model for the atmospheric boundary layer, *J. Meteorol. Soc. Jpn.*, *87*(5), 895–912.
Nielsen, N. W. (1997), An early-autumn polar low formation over the Norwegian Sea, *J. Geophys. Res.*, *102*, 13,955–13,973, doi:10.1029/97JD00281.
Noer, G., and Ø. Saetra (2011), A climatological study of polar lows in the Nordic Seas, *Q. J. R. Meteorol. Soc.*, *137*(660), 1762–1772.
Nordeng, T. E. (1990), A model-based diagnostic study of the development and maintenance mechanism of two polar lows, *Tellus*, *42A*(1), 92–108, doi:10.1034/j.1600-0870.1990.00009.x.
Økland, H. (1987), Heating by organized convection as a source of polar low intensification, *Tellus*, *39A*, 397–407.
Onarheim, I. H., T. Eldevik, M. Årthun, R. B. Ingvaldsen, and L. H. Smedsrud (2015), Skillful prediction of Barents Sea ice cover, *Geophys. Res. Lett.*, *42*, 5364–5371, doi:10.1002/2015GL064359.
Otte, T. L., C. G. Nolte, M. J. Otte, and J. H. Bowden (2012), Does nudging squelch the extremes in regional climate modeling?, *J. Clim.*, *25*, 7046–7066.
Rasmussen, E. (1979), The polar low as an extratropical CISK disturbance, *Q. J. R. Meteorol. Soc.*, *105*(445), 531–549.
Rasmussen, E. (1985), A case study of a polar low development over the Barents Sea, *Tellus*, *37A*(5), 407–418.
Rasmussen, E. A., and J. Turner (2003), *Polar Lows: Mesoscale Weather Systems in the Polar Regions*, Cambridge Univ. Press, Cambridge, U. K.
Sanders, F., and J. R. Gyakum (1980), Synoptic-dynamic climatology of the "Bomb", *Mon. Weather Rev.*, *108*(10), 1589–1606, doi:10.1175/1520-0493(1980)108<1589:SDCOT>2.0.CO;2.
Schultz, D. M., and J. M. Sienkiewicz (2013), Using frontogenesis to identify sting jets in extratropical cyclones, *Weather Forecast.*, *28*(3), 603–613, doi:10.1175/WAF-D-12-00126.1.
Screen, J. A., and I. Simmonds (2010), Increasing fall-winter energy loss from the Arctic Ocean and its role in Arctic temperature amplification, *Geophys. Res. Lett.*, *37*, L16707, doi:10.1029/2010GL044136.
Shapiro, M., L. Fedor, and T. Hampel (1987), Research aircraft measurements of a polar low over the Norwegian Sea, *Tellus*, *39A*(4), 272–306.
Shimada, U., A. Wada, K. Yamazaki, and N. Kitabatake (2014), Roles of an upper-level cold vortex and low-level baroclinicity in the development of polar lows over the Sea of Japan, *Tellus*, *66A*, 24694, doi:10.3402/tellusa.v66.24694.
Simmonds, I., and K. Keay (2009), Extraordinary September Arctic sea ice reductions and their relationships with storm behavior over 1979–2008, *Geophys. Res. Lett.*, *36*, L19715, doi:10.1029/2009GL039810.
Skamarock, W. C., and J. B. Klemp (2008), A time-split nonhydrostatic atmospheric model for weather research and forecasting applications, *J. Comput. Phys.*, *227*(7), 3465–3485, doi:10.1016/j.jcp.2007.01.037.
Smirnova, J. E., P. A. Golubkin, L. P. Bobylev, E. V. Zabolotskikh, and B. Chapron (2015), Polar low climatology over the Nordic and Barents seas based on satellite passive microwave data, *Geophys. Res. Lett.*, *42*, 5603–5609, doi:10.1002/2015GL063865.
Terpstra, A., T. Spengler, and R. W. Moore (2015), Idealised simulations of polar low development in an Arctic moist-baroclinic environment, *Q. J. R. Meteorol. Soc.*, *141*, 1987–1996.
Tewari, M., F. Chen, W. Wang, J. Dudhia, M. LeMone, K. Mitchell, M. Ek, G. Gayno, J. Wegiel, and R. Cuenca (2004), Implementation and verification of the unified NOAH land surface model in the WRF model, paper presented at 20th conference on weather analysis and forecasting/16th conference on numerical weather prediction.
Thompson, G., P. R. Field, R. M. Rasmussen, and W. D. Hall (2008), Explicit forecasts of winter precipitation using an improved bulk microphysics scheme. Part II: Implementation of a new snow parameterization, *Mon. Weather Rev.*, *136*, 5095–5115.
von Storch, H., H. Langenberg, and F. Feser (2000), A spectral nudging technique for dynamical downscaling purposes, *Mon. Weather Rev.*, *128*(10), 3664–3673.
Wang, C.-C., and J. C. Rogers (2001), A composite study of explosive cyclogenesis in different sectors of the North Atlantic. Part I: Cyclone structure and evolution, *Mon. Weather Rev.*, *129*(6), 1481–1499.
Wilhelmsen, K. (1985), Climatological study of gale-producing polar lows near Norway, *Tellus*, *37A*(5), 451–459.

Yanase, W., and H. Niino (2005), Effects of baroclinicity on the cloud pattern and structure of polar lows: A high-resolution numerical experiment, *Geophys. Res. Lett.*, *32*, L02806, doi:10.1029/2004GL020469.

Yanase, W., and H. Niino (2007), Dependence of polar low development on baroclinicity and physical processes: An idealized high-resolution numerical experiment, *J. Atmos. Sci.*, *64*(9), 3044–3067, doi:10.1175/jas4001.1.

Yanase, W., G. Fu, H. Niino, and T. Kato (2004), A polar low over the Japan Sea on 21 January 1997. Part II: A numerical study, *Mon. Weather Rev.*, *132*(7), 1552–1574.

Zahn, M., and H. von Storch (2010), Decreased frequency of North Atlantic polar lows associated with future climate warming, *Nature*, *467*(7313), 309–312, doi:10.1038/nature09388.

Zahn, M., H. Von Storch, and S. Bakan (2008), Climate mode simulation of North Atlantic polar lows in a limited area model, *Tellus*, *60A*(4), 620–631, doi:10.1111/j.1600-0870.2008.00330.x.